

Vertical profiles of cloud condensation nuclei number concentration and its empirical estimate from aerosol optical properties over the North China Plain

Rui Zhang¹, Yuying Wang¹, Zhanqing Li^{2,3}, Zhibin Wang⁴, Russell R. Dickerson³, Xinrong Ren^{3,5}, Hao He³, Fei Wang^{6,5}, Ying Gao^{7,6}, Xi Chen¹, Jialu Xu¹, Yafang Cheng^{8,7}, Hang Su^{9,8}

¹ Key Laboratory for Aerosol-Cloud-Precipitation of China Meteorological Administration, School of Atmospheric Physics, Nanjing University of Information Science & Technology, Nanjing 210044, China

² State Key Laboratory of Remote Sensing Science, College of Global Change and Earth System Science, Beijing Normal University, Beijing 100875, China

³ ~~Earth System Science Interdisciplinary Center~~, Department of Atmospheric and Oceanic Science, University of Maryland, College Park, ~~Maryland~~ **20740**, USA

⁴ Research Center for Air Pollution and Health, College of Environmental and Resource Science, Zhejiang University, Hangzhou 310058, China

⁵ Air Resources Laboratory, National Oceanic and Atmospheric Administration, College Park, Maryland 20740, USA

^{6,5} Key Laboratory for Cloud Physics, Chinese Academy of Meteorological Sciences, Beijing, 100081, China

^{7,6} School of Atmospheric Sciences, Nanjing University, Nanjing 210008, China

^{8,7} Minerva Research Group, Max Planck Institute for Chemistry, 55128 Mainz, Germany

^{9,8} Multiphase Chemistry Department, Max Planck Institute for Chemistry, 55128 Mainz, Germany

Correspondence to: Yuying Wang (yuyingwang@nuist.edu.cn)

带格式的: 缩进: 左侧: 0 厘米, 首行缩进: 0 字符

Abstract

To better understand the characteristics of aerosol activation ability and optical properties, a comprehensive airborne campaign was ~~implemented~~conducted over the North China Plain (NCP) from May 8 to June 11, 2016. Vertical profiles of cloud condensation nuclei (CCN) number concentration (N_{CCN}) and aerosol optical properties were measured simultaneously. Seventy-two-hour air mass back trajectories show that during the campaign the measurement region ~~was~~ mainly influenced by air masses ~~in from the~~ northwest and southeast. Air mass sources, temperature structure, anthropogenic emissions, and terrain distribution are factors influencing N_{CCN} profiles. CCN spectra suggest that the ability of aerosol ~~to activate~~ion into CCN is stronger in southeasterly air masses than in northwesterly air masses and stronger in the free atmosphere than near the surface. Vertical distributions of aerosol scattering Ångström exponent (SAE) indicate that aerosols near the surface mainly originate from primary emissions consisting of more fine particles. The ~~combined effect of aerosol lifting aloft and~~ long-distance transport increases SAE and makes it vary more in the free troposphere than near the surface. ~~For To~~ parameterizing N_{CCN} , the equation $N_{CCN}=10^{\beta} \cdot \sigma^{\gamma}$ is used to fit the relationship between N_{CCN} and the aerosol scattering coefficient (σ) at 450 nm. The fitting parameters β and γ have linear relationships with the SAE. Empirical estimates of N_{CCN} at 0.7% water vapor supersaturation (~~ss~~SS) from aerosol optical properties are thus retrieved for the two air masses: $N_{CCN}=10^{-0.22 \cdot SAE+2.39} \cdot \sigma^{0.30 \cdot SAE+0.29}$ for northwesterly air masses and $N_{CCN}=10^{-0.07 \cdot SAE+2.29} \cdot \sigma^{0.14 \cdot SAE+0.28}$ for southeasterly air masses. The estimated N_{CCN} at 0.7% ~~ss~~SS agrees with that measured, although the performance differs between low and high concentrations in the two air masses. The results highlight the important impact of aerosol sources on the empirical estimate of N_{CCN} from aerosol optical properties.

带格式的: 字体: 非倾斜

带格式的: 字体: Times New Roman

1. Introduction

Defined as the mixture of solid and liquid particles suspended in the air, aerosols have a great impact on Earth's climate system via their direct and indirect effects (IPCC, 2021). They not only alter Earth's radiation budget by absorbing and scattering solar radiation directly (e.g., Bond et al., 2013) but also affect the radiation budget indirectly by serving as cloud condensation nuclei (CCN),

modifying the microphysical properties of clouds (e.g., Lohmann and Feichter, 2005; Andreae and Rosenfeld, 2008). This is referred to as aerosol-cloud interactions (ACI). Many studies suggest that good knowledge of the CCN activation ability is the key to quantitatively evaluating ACI and its radiative forcing in models (e.g., Rosenfeld et al., 2014, 2016; Z. Li et al., 2016, 2019; Liu and Li., 2020). However, this is uncertain because of the lack of comprehensive observations.

CCN is a subset of aerosols that can be activated at a certain water vapor supersaturation (ΔS). The activation ability is mainly determined by three aerosol properties, namely, particle size, chemical composition, and mixing state (e.g., Farmer et al., 2015; F. Zhang et al., 2017; Cai et al., 2018; Y. Wang et al., 2018). Previous studies have reported that these three factors have large spatiotemporal variabilities over different regions in the world (e.g., Juranyi et al., 2011; Paramonov et al., 2015; Schmale et al., 2018), especially in fast-developing countries like China (Z. Li et al., 2019). This increases the uncertainty of estimates of ACI.

To evaluate the effect of aerosols on air quality and atmospheric radiative forcing in China, many field experiments have been carried out in recent years in some developed regions, such as the Pearl River Delta (PRD) (e.g., Rose et al., 2010), the Yangtze River Delta (YRD) (e.g., Leng et al., 2013), and the North China Plain (NCP) (e.g., L. J. Guo et al., 2015; F. Zhang et al., 2017; J. Ren et al., 2018). Some of these studies including measurements of CCN aimed at investigating the characteristics of CCN activation properties and their influential factors that influence them or establishing reasonable estimation schemes for CCN number concentration (N_{CCN}). For example, L. J. Guo et al. (2015) discussed the change in CCN activation properties in a long-lasting severe fog and haze episode. F. Zhang et al. (2017) conducted N_{CCN} closure experiments, finding that N_{CCN} was well estimated using the data of aerosol size number concentration and bulk chemical composition but it was influenced by the aerosol aging level. J. Ren et al. (2018) suggested that it was better to predict N_{CCN} using aerosol size-resolved rather than bulk chemical composition data. However, most of these studies were based on ground-based observations, which could not characterize the vertical distributions of CCN properties and N_{CCN} profiles. The CCN activation ability and N_{CCN} below cloud bases are key in quantifying ACI (Rosenfeld et al., 2014; Z. Li et al., 2016). Therefore, it is necessary to do more studies about CCN profiles in China.

A commonly used platform to observe vertical distributions of N_{CCN} profiles and the vertical distribution of and CCN activation ability is an aircraft (e.g., J. Li et al., 2015b; Jayachandran et al.,

2020a; Manoj et al., 2021; Z. Cai et al., 2022). However, limited by high costs and technological complexity, current aircraft measurements are insufficient to quantify ACI. Some studies have thus attempted to estimate N_{CCN} using aerosol optical data that are much more plentiful (e.g., Andreae, 2009; Liu and Li, 2014; Tao et al., 2018). For example, Andreae (2009) built an exponential function between N_{CCN} and aerosol optical depth (AOD). Liu and Li (2014) found that the relationship between N_{CCN} and AOD becomes invalid when the relative humidity (RH) exceeds 75% and they developed new parameterized relationships to estimate N_{CCN} accounting for RH, particle size, and single scattering albedo (SSA), defined the aerosol scattering index (AI) using aerosol scattering coefficients (σ) and aerosol scattering Ångström exponent (SAE) to estimate N_{CCN} . Tao et al. (2018) established a lookup table that includes σ , hygroscopicity parameter (κ), and Ångström exponent (\AA) for estimating N_{CCN} based on the measurement of a three-wavelength humidified nephelometer system. The vertical profiles of N_{CCN} were also predicted using lidar data. For example, Mamouri and Ansmann (2016) investigated the potential of polarization lidar data to estimate vertical distributions of N_{CCN} . Lv et al. (2018) developed an algorithm for profiling N_{CCN} using backscatter coefficients at 355, 532, and 1,064 nm and extinction coefficients at 355 and 532 nm from multiwavelength lidar systems. Satellite lidar data of the Cloud–Aerosol Lidar and Infrared Pathfinder Satellite Observations (CALIPSO) have also been employed to retrieve the profiles of lidar of CCN (Choudhury and Tesche 2022). Most of the retrieved N_{CCN} profiles are yet to be validated against in situ N_{CCN} profile measurements. Most of these N_{CCN} parameterization schemes, however, were conducted based on ground-based observations in different regions and were rarely verified by in situ N_{CCN} profiles.

Over the past few decades, rapid industrialization and urbanization have made the NCP one of the most heavily polluted regions in China. The large number of aerosols and gases emitted by human activities deteriorated air quality, strongly impacting the regional climate (e.g., Fan et al., 2016; Chen et al., 2022). The aerosol activation ability and optical properties in the NCP have drawn much attention (e.g., Zhang et al., 2016, 2017; Wang et al., 2018b). In light of this, we undertook a comprehensive airborne campaign in the NCP under the aegis of a project called Air chemistry Research In Asia (ARIAs). We directly measured profiles of N_{CCN} and aerosol optical properties from an aircraft and analyzed the CCN activation property and relationships between N_{CCN} and aerosol optical properties. The in-situ measurements presented here are beneficial in validating lidar

带格式的: (中文), (其他)

带格式的: (中文), (其他), 非上标/下标

带格式的: (中文), (其他)

带格式的: 字体: (默认) Times New Roman, (中文) 宋体, 五号, 字体颜色: 文字 1, (中文), (其他), 图案: 清除

带格式的: (中文), (其他)

带格式的: 字体: 倾斜

带格式的: 字体: (默认) Times New Roman, (中文) 宋体, 五号, 字体颜色: 文字 1, (中文), (其他), 图案: 清除

带格式的: 字体: (中文) 宋体, 五号, (中文), (其他)

带格式的: 字体: (默认) Times New Roman, (中文) 宋体, 五号, 字体颜色: 文字 1, (中文), (其他), 图案: 清除

带格式的: 字体: (默认) Times New Roman, (中文) 宋体, 五号, 字体颜色: 文字 1, (中文), (其他), 图案: 清除

带格式的: 字体: (默认) Times New Roman, (中文) 宋体, 五号, 字体颜色: 文字 1, (中文), (其他), 图案: 清除

带格式的: 字体: (默认) Times New Roman, (中文) 宋体, 五号, 字体颜色: 文字 1, (中文), (其他), 图案: 清除

带格式的: 字体: (默认) Times New Roman, (中文) 宋体, 五号, 字体颜色: 文字 1, (中文), (其他), 图案: 清除

带格式的: 字体: (默认) Times New Roman, (中文) 宋体, 五号, 字体颜色: 文字 1, (中文), (其他), 图案: 清除

带格式的: 字体: (默认) Times New Roman, (中文) 等线, 10磅, 字体颜色: 文字 1

带格式的: 字体: (默认) Times New Roman, (中文) 等线, 10磅, 字体颜色: 文字 1

带格式的: 字体: (默认) Times New Roman, (中文) 等线, 10磅, 字体颜色: 文字 1

带格式的: 字体: (默认) Times New Roman, (中文) 等线, 10磅, 字体颜色: 文字 1

带格式的: 字体颜色: 自动设置

带格式的: 字体: (中文) 宋体, 字体颜色: 文字 1, (中文), (其他)

带格式的: 字体: (中文) 宋体, 字体颜色: 文字 1, (中文), (其他)

or satellite-based N_{CCN} retrieval algorithms (e.g., Choudhury and Tesche, 2022). Moreover, This study will provide a perspective to improve aerosol-cloud parameterizations applied in the NCP. Analytical methods developed here will also be applicable to other regions of the world.

This paper is structured as follows. Details about the airborne campaign, instruments, and air mass sources are given in Section 2. Section 3 discusses and analyzes N_{CCN} profiles at 0.7% ss_{SS} , vertical distributions of CCN spectra, and possible relationships between N_{CCN} and aerosol optical properties. Section 4 summarizes the major conclusions of this study.

2. Airborne campaign, instruments, and air mass sources

2.1 Airborne campaign

Hebei province (36°05' N-42°40' N, 113°27' E-119°50' E) is located north of the Yellow River and east of the Taihang Mountains in the NCP. It surrounds the Beijing and Tianjin megacities, and borders Shangdong province to the east, Shanxi province to the west, Henan province to the south, and the Inner Mongolia Autonomous Region to the north (Fig. 1a). The terrain of Hebei province is high in the northwest and low in the southeast, with the altitude generally decreasing from the northwest to the southeast. The plain area covers most of Hebei province, located in the eastern foothills of the Taihang Mountains.

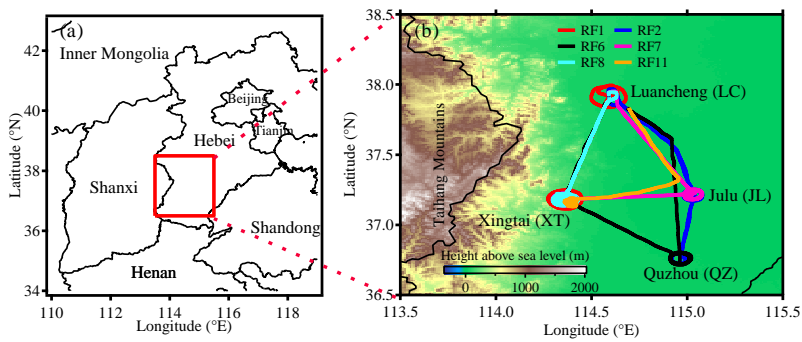


Figure 1. (a) The geographic location of Hebei province and **(b)** flight tracks of six flights conducted over the southern plain of Hebei province in from May 8 to June 11, 2016. The colored background shows terrain heights above sea level (unit: m). The number after ‘RF’ indicates the research flight number.

The ARIAs campaign was carried out from May 8 to June 11, 2016 in the southern plain area of Hebei province using a Y-12 turboprop airplane operated by the Weather Modification Office of the Hebei Meteorological Bureau. The details of the flight plans, and initial investigations into the impact of air mass on air chemistry have been published (Benish et al., 2020, 2021; F. Wang et al., 2018), were introduced in F. Wang et al. (2018). The sampling method was summarized in the supplement. The influence of air mass and regional transport as MAX-DOAS and LIDAR has been presented (Wang et al., 2019). This previous work identified coal combustion, industrial processes, vehicular traffic, and biomass burning as contributors to poor air quality. Luancheng (LC, 114.36° E, 37.18° N; 182 m above mean sea level, or a.s.l.), Xingtai (XT, 114.36° E, 37.18° N; 182 m a.s.l.), Julu (JL, 115.02° E, 37.22° N; 20 m a.s.l.), and Quzhou (QZ, 114.96° E, 36.76° N; 40 m a.s.l.) are the four central sampling sites (Fig. 1b), all to the east of the Taihang Mountains. Six flights (RF1, RF2, RF6, RF7, RF8, and RF11) measuring N_{CCN} and aerosol optical properties are used in this study. In all the flights, the Y-12 airplane conducted vertical spiral flights from ~0.3 to ~3.5 km near one or two central sampling sites and level flights at different fixed altitudes between different central sampling sites. Every flight obtained several N_{CCN} profiles at one or two sites and N_{CCN} data at several fixed altitudes. Table 1 lists details about the flight tracks (also see Fig. 1b).

Altitudes are distances a.s.l. in this study. All aircraft flights except RF8 (conducted from 16:30–18:24 CST; CST stands for China standard time, which is 8h ahead of UTC) were conducted around noon (10:00–15:00 CST), when the planetary boundary layer (PBL) height was fully developed.

Table 1. Detailed information about the flight tracks deployed during the campaign. Flight code (third column): The number after ‘RF’ indicates the research flight number, the number after ‘_’ indicates the number of vertical spiral flights, and the letter after ‘_’ indicates the number of level transects. flights.

Flight number, date	Time range (CST)	Flight code	Region covered	Vertical height a.s.l. (km)	Sampling duration (min)	Maximum spiral radius (km)
		RF1_1	XT	0.3–3.7	38	~40

带格式的: 字体颜色: 自动设置

带格式的: 字体颜色: 自动设置, 非突出显示

带格式的: 字体颜色: 自动设置

带格式的: 字体: (默认) Times New Roman, (中文) 宋体, 五号, 字体颜色: 自动设置, 英语(美国), 不检查拼写或语法

带格式的: 字体: (默认) Times New Roman, (中文) 宋体, 五号, 字体颜色: 自动设置, 不检查拼写或语法

带格式的: 字体颜色: 自动设置

带格式的: 字体颜色: 自动设置, 非突出显示

带格式的: 字体颜色: 自动设置, 非突出显示

带格式的: 字体颜色: 自动设置

带格式的: 字体颜色: 自动设置, 非突出显示

带格式的: 字体颜色: 自动设置

带格式的: 缩进: 左 0 字符, 首行缩进: 0 字符

带格式的: 居中

带格式表格

带格式的: 缩进: 左侧: 0 厘米, 悬挂缩进: 1 字符, 首行缩进: -1 字符

带格式的: 居中

RF1, 20160508	13:02– 14:29	RF1_a RF1_2	track from XT to LC LC	~3.6 0.3–3.2	<u>20</u> <u>15</u>	<u>~4.0</u>	带格式的: 字体: (中文) + 中文正文 (等线)
RF2, 20160515	12:17– 15:04	RF2_a	track from LC to JL	~0.4	<u>18</u>	<u>~5.0</u>	带格式的: 居中
		RF2_1	JL	0.3–3.6	<u>40</u>	<u>~5.0</u>	带格式的: 字体: (中文) + 中文正文 (等线)
		RF2_2	QZ	0.3–3.6	<u>38</u>	<u>~5.0</u>	带格式的: 居中
		RF2_b	track from QZ to JL	~3.6	<u>7</u>	<u>~5.0</u>	带格式的: 居中
		RF2_c	track from JL to LC	~0.4	<u>10</u>	<u>~5.0</u>	带格式的: 居中
RF6, 20160521	12:04– 14:41	RF6_1	QZ	0.3–3.1	<u>36</u>	<u>~5.0</u>	带格式的: 字体: (中文) + 中文正文 (等线)
		RF6_a	track from QZ to XT	~2.5	<u>18</u>	<u>~5.0</u>	带格式的: 居中
		RF6_2	XT	0.3–2.6	<u>43</u>	<u>~5.0</u>	带格式的: 字体: (中文) + 中文正文 (等线)
		RF6_b	track from XT to LC	~1.1	<u>13</u>	<u>~5.0</u>	带格式的: 居中
RF7, 20160528	10:21– 13:25	RF7_a	track around XT	~3.1	<u>20</u>	<u>~5.0</u>	带格式的: 字体: (中文) + 中文正文 (等线)
		RF7_1	XT	0.5–3.1	<u>49</u>	<u>~5.0</u>	带格式的: 居中
		RF7_b	track from XT to JL	~0.4	<u>10</u>	<u>~5.0</u>	带格式的: 居中
		RF7_2	JL	0.3–2.5	<u>26</u>	<u>~4.0</u>	带格式的: 字体: (中文) + 中文正文 (等线)
		RF7_c	track from JL to LC	~1.8	<u>7</u>	<u>~5.0</u>	带格式的: 居中
RF8, 20160528	16:30– 18:24	RF8_a	track around XT	~0.6	<u>15</u>	<u>~5.0</u>	带格式的: 字体: (中文) + 中文正文 (等线)
		RF8_1	XT	0.5–3.1	<u>36</u>	<u>~5.0</u>	带格式的: 居中
RF11, 20160611	11:07– 12:28	RF11_a	track around XT	~0.6	<u>16</u>	<u>~5.0</u>	带格式的: 居中
		RF11_1	XT	0.3–3.2	<u>50</u>	<u>~4.0</u>	带格式的: 字体: (中文) + 中文正文 (等线)

168		带格式的: 居中
169	2.2 Instruments	带格式的: 居中
170	To satisfy the needs of this study, the Y-12 airplane was equipped with a dual-column CCN	带格式的: 字体: (中文) + 中文正文 (等线)
171	counter (CCNc), a three-wavelength integrating nephelometer, and a Cloud Water Inertial Probe	带格式的: 居中
172	(CWIP). All instruments were calibrated rigorously prior to the airborne campaign. Table 2	带格式的: 居中
173	summarizes the instruments equipped on the airplane.	带格式的: 字体: (中文) + 中文正文 (等线)
174		带格式的: 居中
175		带格式的: 居中

Table 2. Instruments equipped on the Y-12 airplane used in this study.

Instrument	Parameter	Time resolution	Accuracy
CCN counter			
(model CCNc-200, DMT Inc.)	CCN number concentrations (N_{CCN})	1 s	—
Nephelometer			
(model 3565, TSI Inc.)	Aerosol scattering coefficients (σ) at three wavelengths (450, 550, and 700 nm)	1 s	0.5 Mm ⁻¹
CWIP			
(Rain Dynamics Inc.)	Temperature (T)	1 s	1 K
	Relative humidity (RH)	1 s	2%
	Position	0.1 s	—

177 N_{CCN} was measured by a dual-column continuous-flow thermal-gradient cloud condensation
 178 nuclei counter (model CCNc-200, DMT Inc.) with a time resolution of 1 s. It is equipped with
 179 two columns that can simultaneously measure N_{CCN} at two different ~~ss~~SS levels without mutual
 180 interference. In this campaign, only one ~~ss~~SS level is set in the first column during all flights, but
 181 eight different ~~ss~~SS levels are set in the second column with a measurement time interval of 90 s
 182 for each ~~ss~~SS level. ~~The CCNc data with instable sample or sheath flow is excluded.~~ Considering
 183 the time reaching equilibrium at different time of ss levels, data acquired in the final 30 s ~~data~~
 184 at any ~~ss~~SS level in the cycle for the second column is used in this study. The ~~ss~~SS level in columns
 185 was calibrated with pure ammonium sulfate following procedures developed by Rose et al. (2008).
 186 The ~~ss~~SS level in the first column was corrected to 0.7% and the ~~ss~~SS levels in the second column
 187 were corrected to 0.44%, 0.56%, 0.68%, 0.80%, 0.92%, 1.04%, 1.16%, and 1.28%. N_{CCN} profiles
 188 at 0.7% ~~ss~~SS and N_{CCN} data at different ~~ss~~SS levels were thus available.

带格式的: 非上标/下标

带格式的: 字体颜色: 自动设置

189 The integrating nephelometer (model 3565, TSI Inc.) can continuously measure aerosol
 190 scattering coefficients (σ) at three wavelengths (450, 550, and 700 nm) with a time resolution of 1
 191 s. Previous studies have shown that σ becomes larger with increasing relative humidity (RH) due
 192 to aerosol hygroscopic growth (e.g., L. Zhang et al., 2015; R. Ren et al., 2021). Hence, ~~the~~
 193 ~~scattering values were adjusted using a correction factor (Anderson and Ogren, 1998) the RH of~~
 194 ~~sampled air was dried to below 40% in this campaign.~~ The nephelometer was calibrated and tested
 195 rigorously prior to the airborne campaign using carbon dioxide gas and filtered zero air. Anderson
 196 and Ogren (1998) have provided details about the calibration methods and measurement
 197 uncertainties of ~~integrating this~~ nephelometer. The Aerosol scattering Ångström exponent (SAE) is
 198 calculated as follows, where $\sigma(\lambda_1)$ and $\sigma(\lambda_2)$ are aerosol scattering coefficients at two given
 199 wavelengths ($\lambda_1 = 450$ nm and $\lambda_2 = 700$ nm).

带格式的: 缩进: 左 0.5 字符, 首行缩进: 2 字符

带格式的: 字体: (默认) Times New Roman, (中文) 宋体, 五号, 字体颜色: 文字 1

带格式的: 字体: (默认) Times New Roman, (中文) 宋体, 五号, 字体颜色: 文字 1

带格式的: 字体: (默认) Times New Roman, (中文) 宋体, 五号

带格式的: 字体: 非倾斜, 字体颜色: 自动设置

带格式的: 字体颜色: 自动设置

带格式的: 字体: 非倾斜, 字体颜色: 自动设置

带格式的: 字体颜色: 自动设置

带格式的

200
$$SAE = \frac{\log(\sigma(\lambda_1)) - \log(\sigma(\lambda_2))}{\log(\lambda_1) - \log(\lambda_2)} \quad (1)$$

 201 SAE is often used to qualitatively assess the dominant size mode of aerosols, reflecting the
 202 particle number size distribution (PNSD) pattern (e.g., Hamonou et al., 1999). A large SAE (> 2)
 203 generally implies that fine-mode aerosols dominated are dominant (e.g., smoke particles), while a
 204 small SAE (< 1) means that the coarse mode are dominant dominated (e.g., dust particles).

带格式的

带格式的: 缩进: 左 0.5 字符, 首行缩进: 2 字符

带格式的: 字体: 加粗

Ambient temperature (T) and RH were measured by a CWIP (Rain Dynamics Inc.) with a time resolution of 1 s during flights. Real-time flight position data such as longitude, latitude, and altitude were recorded by a global positioning system (GPS) and the CWIP with a time resolution of 0.1 s. The CWIP time was calibrated and synchronized with the GPS time prior to deployment.

2.3 Air mass sources

Previous studies have suggested that differences in air masses will lead to spatiotemporal differences in CCN activation ability and aerosol optical properties (e.g., Xu et al., 2020; Jayachandran et al., 2020b). To better understand air mass sources and aerosol transport pathways over the measurement area, seventy-two-hour air mass back trajectories for all N_{CCN} profiles at 0.5, 1.5, 2.5, and 3.5 km are analyzed using the NOAA Hybrid Single Particle Lagrangian Integrated Trajectory (HYSPLIT) model (Stein et al., 2021; Draxler and Hess, 1998). Results show that the sampling region is mainly influenced by two distinct air masses, namely, northwesterly air masses and southeasterly air masses (Fig. 2). Northwest~~erly~~ air masses (Fig. 2a) originate from arid or semi-arid land, including five N_{CCN} profiles whose flight codes are RF1_1, RF1_2, RF2_1, RF2_2, and RF11_1. Before these trajectories approach the sampling area, most of these air masses flow around or are forced to lift due to the influence of the Taihang Mountains. However, southeasterly air masses (Fig. 2b) originate from coastal or marine areas, also including five N_{CCN} profiles whose flight codes are RF6_1, RF6_2, RF7_1, RF7_2, and RF8_1. Air masses in place during the RF7_1, RF7_2, and RF8_1 flights originate from coastal areas, and those during the RF6_1 and RF6_2 flights originate from the western Pacific. Southeast trajectories pass over the densely populated plain region to the east and south of the sampling area, which is easily impacted by anthropogenic emissions. These trajectories are also easily affected by differences in land and sea thermal properties, raising the air masses gradually before reaching the sampling area (Fig. S1).

带格式的: 字体: (中文) NimbusRomNo9L-Regu, 五号

带格式的: 字体: (中文) NimbusRomNo9L-Regu

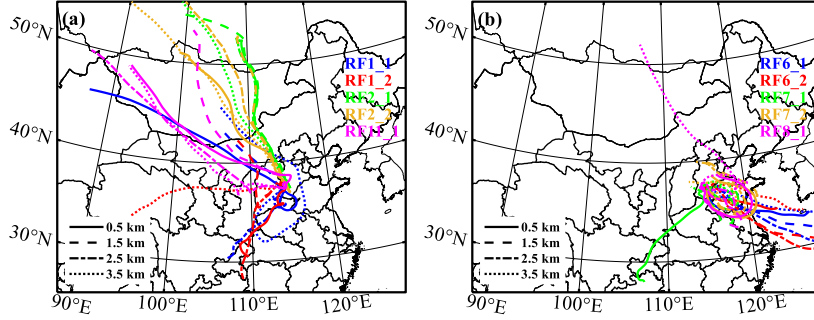


Figure 2. Seventy-two-hour HYSPLIT back trajectories over the sampling region: (a) northwesterly air masses and (b) southeasterly air masses. The color of trajectories indicates different flight codes associated with N_{CCN} profiles. The line type shows trajectories with different starting altitudes (0.5, 1.5, 2.5, and 3.5 km).

3. Results and Discussion

3.1 Vertical distributions of N_{CCN}

3.1.1 Effect of the temperature inversion layer (TIL) on N_{CCN} profiles

Previous studies have demonstrated the significant impact of the TIL structure on the vertical distributions of aerosols and N_{CCN} (e.g., Janhäll et al., 2006; J. Li et al., 2015a, 2015b). Here, N_{CCN} profiles are classified into three categories according to the number of TILs (Table 3). Three typical N_{CCN} profiles at 0.7% ss-SS (RF2_1, RF6_1, and RF1_1) with different numbers of TILs are chosen for comparison purposes (Fig. 3; N_{CCN} profiles associated with the other three flight codes are shown in Figs. S2–4).

Table 3. Classification of different N_{CCN} profiles based on the number of TILs.

Categories	Flight codes of N_{CCN} profiles
No TIL	RF2_1, RF2_2
One TIL	RF6_1, RF6_2, RF7_1, RF7_2, RF8_1, RF11_1
Two TILs	RF1_1, RF1_2

No TIL: Figure 3a shows vertical profiles of T and potential temperature (θ) for the RF2_1 N_{CCN} profile (Fig. 3b). T decreases with altitude in the absence of a TIL while the variation in θ with

altitude ($\partial\theta/\partial z$) is generally small below ~ 2.3 km (Fig. 3a). These meteorological conditions are favorable for the upward transport of aerosols below ~ 2.3 km. The larger $\partial\theta/\partial z$ above ~ 2.3 km suggests a more stable atmosphere, suppressing the upward transport of aerosols (Yau and Rogers, 1998). This is why N_{CCN} peaks at ~ 2.3 km and decreases rapidly above (Fig. 3b). However, a second N_{CCN} peak is observed at ~ 3.2 km, with a small $\partial\theta/\partial z$ in the vicinity. The seventy-two-hour back trajectory shows that the air mass in this case originates from the northwestern arid/semi-arid parts of Mongolia (Fig. 2a). The long-distance transport of aerosols (like dust particles) may be responsible for the N_{CCN} peak at ~ 3.2 km. In another N_{CCN} profile with no TIL (RF2_2), a weak N_{CCN} peak also appears at ~ 3.2 km (Fig. S2b). The RF11_1 N_{CCN} profile with similar back trajectories as RF2_1 and RF2_2 also has a weak N_{CCN} peak at ~ 3.2 km. This suggests that the long-distance transport of aerosols plays an important role in N_{CCN} in the free troposphere over the NCP under the influence of northwesterly air masses. Note that high N_{CCN} in the free troposphere has an important impact on cloud microphysical properties (Rosenfeld et al., 2008).

One TIL: The temperature profile in Fig. 3c shows a ~ 0.4 -km-deep TIL at ~ 1.8 km. A thick TIL hinders the upward transport of aerosols and facilitates the vertical mixing of N_{CCN} below the TIL. N_{CCN} thus varies little with altitude below the TIL, with a mean N_{CCN} at 0.7% ~~ss~~ ~~SS~~ of 5140 cm^{-3} (Fig. 3d). The θ profile in Fig. 3c suggests that $\partial\theta/\partial z$ above the TIL is much larger than below the TIL, meaning a more stable atmosphere above the TIL. N_{CCN} quickly decreases by an order of magnitude from below to above the TIL (from 5542 cm^{-3} at ~ 1.8 km to 365 cm^{-3} at ~ 2.2 km). Overall, the presence of a thick TIL has a large impact on the N_{CCN} profile.

Two TILs: The temperature profile in Fig. 3e depicts two shallow TILs with the same depth of ~ 0.2 km, appearing at ~ 0.8 km and ~ 2.5 km, respectively. Due to the hindering effect of a TIL on the vertical transport of aerosols, only a small amount of CCN break through the first TIL and diffuse to higher altitudes. Figure 3f suggests that N_{CCN} increases with altitude from near the surface to the bottom of the first TIL. A large amount of CCN accumulate below the first TIL, peaking at its bottom. The second TIL makes N_{CCN} accumulate again between the two TILs. Under the combined effect of two TILs, the upward transport of CCN becomes difficult. The θ profile in Fig. 3e also shows that $\partial\theta/\partial z$ is always positive, varying slightly with height. N_{CCN} generally experiences a declining trend with altitude between the two TILs (from 6380 cm^{-3} at 0.9 km to 635 cm^{-3} at 2.5 km). Above the second TIL, N_{CCN} remains at low and stable, with concentrations on the order of 10^2 cm^{-3} .

In summary, the TIL structure has an important impact on the vertical distribution of N_{CCN} . Moreover, N_{CCN} in the free troposphere are easily impacted by the long-distance transport of aerosols under the influence of northwesterly air masses.

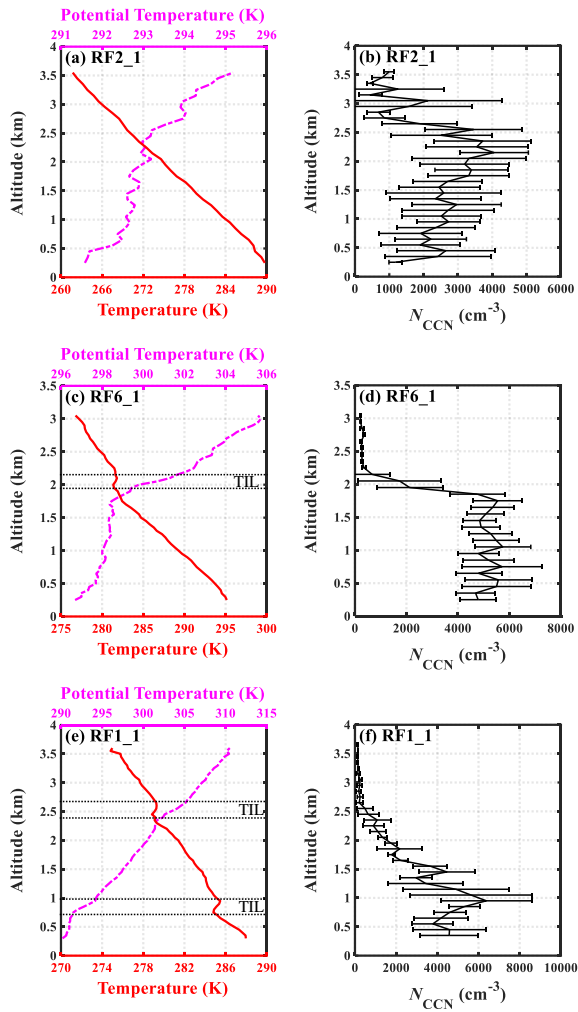


Figure 3. Vertical distributions of temperature (T) and potential temperature (θ) (a, c, e), and N_{CCN} at 0.7% \pm SS (b, d, f) for RF2_1, RF6_1, and RF1_1. N_{CCN} profiles with (from top to bottom) no temperature inversion layer (TIL), one TIL, and two TILs. T and θ are averaged in the intervals of 50 m in altitude. Horizontal error bars of N_{CCN} represent standard deviations of N_{CCN} at 0.7% \pm SS at altitude intervals of 100 m.

带格式的: 字体颜色: 自动设置

带格式的: 字体: 倾斜, 字体颜色: 自动设置

带格式的: 字体颜色: 自动设置

带格式的: 字体: 倾斜, 字体颜色: 自动设置

带格式的: 字体颜色: 自动设置

3.1.2 Influence of air masses on N_{CCN} profiles

To further investigate the influence of air masses on N_{CCN} profiles, the mean N_{CCN} at 0.7% ΔSS in different altitude ranges in two distinct air masses is analyzed (Fig. 4). In general, the mean N_{CCN} at 0.7% ΔSS has a declining trend with increasing altitude in both air masses (Fig. 4a). The N_{CCN} in southeasterly air masses is higher than in northwesterly air masses below 1.5 km, indicating more aerosol particles that can be activated as CCN in southeasterly air masses. Section 2.3 indicates that southeasterly air masses always pass over the densely populated plain area. This means that massive anthropogenic emissions can clearly increase N_{CCN} near the surface. However, N_{CCN} above 2 km is much lower in southeasterly air masses than in northwesterly air masses. This further indicates that the long-range transport of aerosols under the influence of northwesterly air masses contributes significantly to N_{CCN} in the free troposphere.

Figures 4b and 4c depict the mean N_{CCN} at 0.7% ΔSS in different altitude ranges in northwest and southeasterly air masses, respectively. Under the influence of northwesterly air masses, the temperature structure varies, leading to different N_{CCN} profiles (Fig. 4b). For RF2_1 and RF2_2 N_{CCN} profiles with no TIL (Figs. 3b and S2b), the combined effect of upward and long-distance transport of aerosols increases N_{CCN} at 0.7% ΔSS above 2 km. The N_{CCN} from 2 to 2.5 km is even higher than near the surface. For the RF11_1 N_{CCN} profile with one TIL, N_{CCN} at 0.7% ΔSS varies slightly with altitude. For RF1_1 and RF1_2 N_{CCN} profiles with two TILs, N_{CCN} at 0.7% ΔSS above 2 km is much lower than near the surface.

Under the influence of southeasterly air masses, the thermal structure for all N_{CCN} profiles is similar, with one TIL (Table 3). The N_{CCN} profile patterns are thus similar, showing much lower N_{CCN} above 2 km than near the surface (Fig. 4c). Figure 4c also suggests that N_{CCN} at 0.7% ΔSS below 2 km is higher in the RF6_1 and RF6_2 N_{CCN} profiles than in the other three N_{CCN} profiles (i.e., RF7_1, RF7_2, and RF8_1). As discussed in section 2.3, air masses during RF6_1 and RF6_2 originate from the western Pacific, while the others originate from coastal areas. All these air masses pass over the densely populated area before reaching to the measurement region. This suggests that the impact of marine aerosols, biomass burning, and fossil fuel combustion is the possible reasons for high N_{CCN} in the RF6_1 and RF6_2 N_{CCN} profiles. Figure 4c also shows that the N_{CCN} below 2 km is much higher at XT than at QZ and JL during the same flights (RF6_2 vs. RF6_1, and RF7_1

vs. RF7_2). Figure 1b shows that the XT site is closer to the Taihang Mountains than the QZ and JL sites. This implies that the terrain blocking effect of the Taihang Mountains on aerosols accumulates aerosols, resulting in higher N_{CCN} at XT.

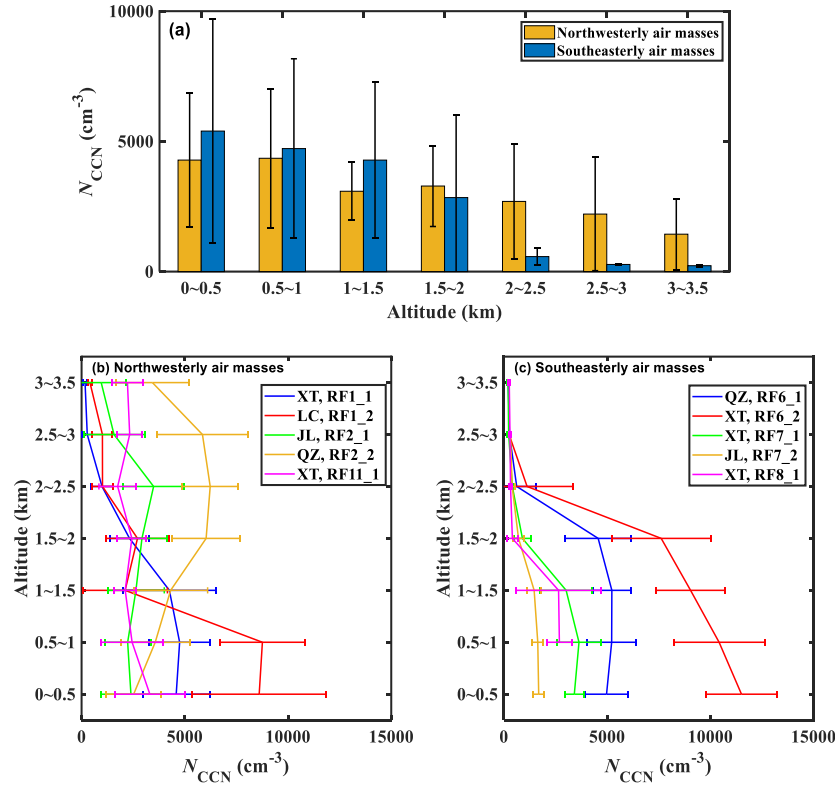


Figure 4. (a) Mean N_{CCN} at 0.7% \pm SS in different altitude ranges (ranging from 0 to 3.5 km at intervals of 0.5 km) in northwesterly and southeasterly air masses, and for different N_{CCN} profiles at 0.7% \pm SS in (b) northwesterly air masses and (c) southeasterly air masses. The different colors in (b) and (c) are for different flights. Error bars represent standard deviations of N_{CCN} at 0.7% \pm SS.

In summary, N_{CCN} profiles are influenced by multiple factors over the NCP. TIL structure, aerosol long-range transport, and anthropogenic emissions lead to differences in the N_{CCN} profiles in different air masses. Even in the same air mass, diverse aerosol sources and terrain distributions cause large differences in N_{CCN} .

3.2 Vertical distributions of CCN spectra in different air masses

The CCN spectrum is usually defined as a function of N_{CCN} to SS . Twomey (1959) first reported ~~an exponential relationship between that N_{CCN} had an exponential relationship with and SS .~~ Since then, a variety of such functions have been proposed thanks to a large number of observations made which are all necessary given its nature of empirical relationships whose validity are generally limited. For example, Ji and Shaw (1998) provided a three-parameter function, while Gunthe et al. (2011) suggested a logarithmic function to fit CCN spectra. In this study, N_{CCN} measurements made at different SS during 11 level flights are used to fit CCN spectra. Twomey's relation (Twomey, 1959; Cohard et al., 1998) is used to fit the relationship between N_{CCN} and SS according to the least-squares method:

$$N_{CCN}(SS) = C \cdot (SS)^k \quad (2)$$

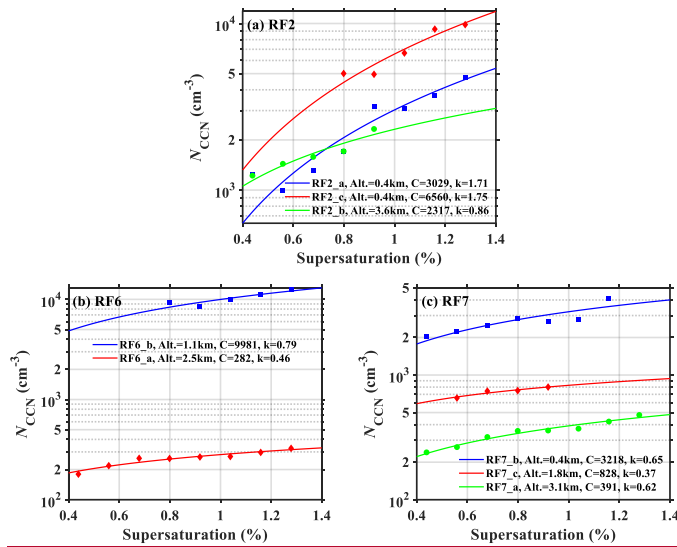
where $N_{CCN}(SS)$ is the N_{CCN} at a specified SS , and C and k are two fitting coefficients. Table S1 lists the fitting results for the 11 level flights. In Eq. (1), the C value represents N_{CCN} at 1.0% SS , and the shape of the CCN spectrum is determined by the k value. Previous studies have suggested that k is closely related to the shape of ~~particle number size distribution (PNSD)~~ and aerosol hygroscopicity (e.g., Hegg et al., 1991; Jefferson, 2010). A lower k value means a stronger aerosol activation ability (i.e., more coarse-mode particles or stronger aerosol hygroscopicity), and vice versa.

Figure 5 shows CCN spectra at different altitudes during three level flights (RF2, RF6, and RF7). The seventy-two-hour back trajectories (Fig. 2a) suggest that the RF2 flight is influenced by northwesterly air masses. The CCN spectra during three level flights (RF2_a, RF2_b, and RF2_c; Fig. 5a) shows that C and k are lower at 3.6 km (RF2_b) than at 0.4 km (RF2_a and RF2_c), indicating smaller N_{CCN} but stronger aerosol activation ability in the free atmosphere than near the surface. At the same altitude (0.4 km), C during the RF2_c flight (6560 cm^{-3}) is more than two times that during the RF2_a flight (3029 cm^{-3}), with different k values (1.75 and 1.71, respectively). This indicates the regional variation of N_{CCN} and the weak aerosol activation ability near the surface.

Figures 5b and 5c show CCN spectra during flights RF6 and RF7, which are influenced by southeasterly air masses (Fig. 2b). The k values associated with southeasterly air masses (Fig. 5b and 5c) are always lower than those associated with northwesterly air masses (Fig. 5a). Therefore, aerosols in southeasterly air masses have a stronger activation ability than those in northwesterly air

masses. This is likely because aerosols from the southeast are mostly from anthropogenic emissions including more secondary particle matters such as sulfate and nitrate, while from the northwest contains more natural components such as mineral dust (Xia et al., 2019; Q. Wang et al., 2022). Figure 5c also shows that k during the RF7 flight decreases from 0.65 at 0.4 km to 0.37 at 1.8 km, increasing to 0.62 at 3.1 km. Figures S3c and S3e show that the altitude of the TIL during the RF7 flight is ~ 2 km. This suggests that the aerosol activation ability near the TIL is stronger than that near the surface and in the free atmosphere above the TIL. This implies that the hindering effect of the TIL promotes aerosol aging processes, enhancing the aerosol activation ability (Y. Wang et al., 2018).

Overall, CCN spectra clearly varies with altitude over the NCP. The fitting coefficients of CCN spectra (C and k) are closely related to air mass sources, regional aerosol properties, and temperature structure.



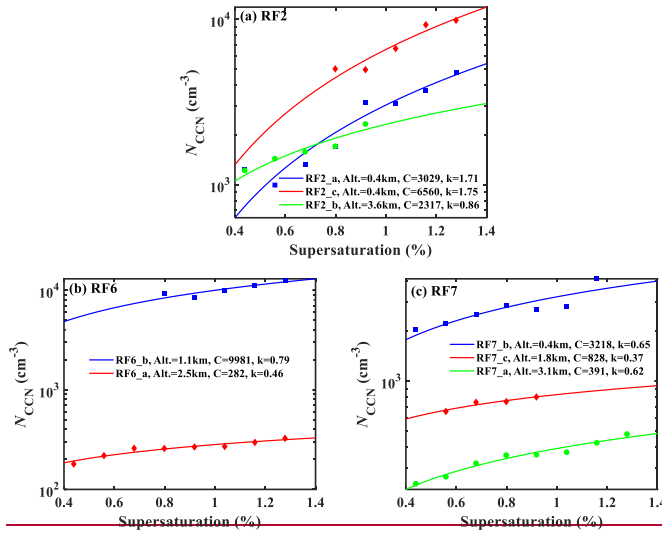


Figure 5. Fitted CCN spectra at different altitudes during three flights: (a) RF2, (b) RF6, and (c) RF7. The flight code, flight altitude (Alt.), and the two fitting coefficients from Twomey's relation (C and k) are given in each panel. Solid lines are the fitting lines described by Eq. (1). The y-axis is logarithmic.

3.3 The relationship between N_{CCN} and aerosol optical properties

3.3.1 Vertical distributions of aerosol scattering Ångström exponent (SAE)—

~~The SAE is calculated as follows, where $\sigma(\lambda_1)$ and $\sigma(\lambda_2)$ are aerosol scattering coefficients at two given wavelengths ($\lambda_1=450$ nm and $\lambda_2=700$ nm)~~

$$SAE = \frac{\log(\sigma(\lambda_1)) - \log(\sigma(\lambda_2))}{\log(\lambda_1) - \log(\lambda_2)} \quad (3)$$

~~SAE is often used to qualitatively assess the dominant size mode of aerosols, reflecting the PNSD pattern (e.g., Hamonou et al., 1999). A large SAE (> 2) generally implies that fine mode aerosols dominated (e.g., smoke particles), while a small SAE (< 1) means that the coarse mode dominated (e.g., dust particles).~~

Figure 6a shows the vertical distributions of SAE during the vertical spiral flights. Three profiles (RF2_1, RF2_2, and RF11_1) are not shown due to the lack of aerosol optical data. In general, SAE decreases gradually with altitude, while its standard deviation increases with altitude. This is likely

带格式的: 缩进: 首行缩进: 0 厘米

because aerosols near the surface are easily influenced by primary emissions from anthropogenic sources, consisting of more fine particles. The frequent appearance of a TIL at ~2 km suppresses the upward transport of fine particles, leading to the rapid decrease of SAE above the TIL. The long-distance transport of coarse-mode aerosols (like dust particles) also decreases SAE in the free troposphere. As mentioned before, aerosol sources above 2 km are complex, which is why the standard deviation of SAE is larger above ~2 km.

Figure 6b shows profiles of N_{CCN} and σ (data used here were collected at 0.7% ss-SS and 450 nm, respectively) during the RF1_1 spiral flight. Figure S5 shows profiles from the other spiral flights. In general, the vertical variation of σ is synchronous with that of N_{CCN} , indicating that they are correlated to some degree.

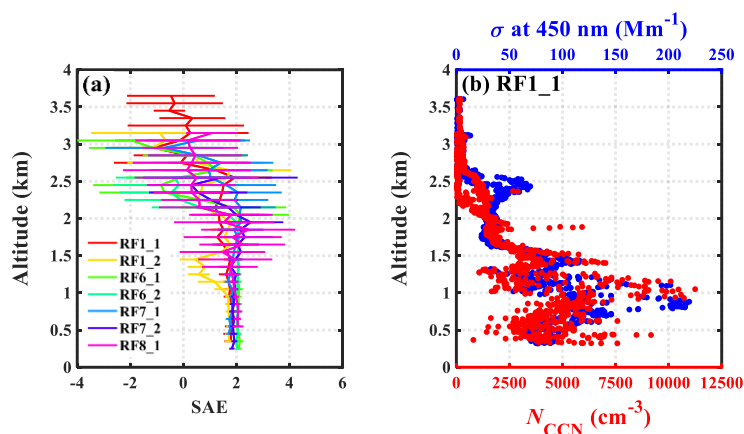


Figure 6. Vertical distributions of (a) aerosol scattering Ångström exponent (SAE) during the vertical spiral flights (error bars are standard deviations of SAE) and (b) N_{CCN} at 0.7% ss-SS (red dots) and aerosol scattering coefficient (σ) at 450 nm (blue dots) during the RF1_1 vertical spiral flight.

3.3.2 Parametrizing Estimation of N_{CCN} from in terms of aerosol optical properties

Both N_{CCN} and aerosol optical properties are affected by the same factors (e.g., PNSD and chemical composition). Therefore, numerous studies attempted to estimate N_{CCN} for aerosol optical properties, although there was no directly physical connection between them (e.g., Andreae, 2009; Liu and Li, 2014; Tao et al., 2018). Previous studies indicated that the relationship between N_{CCN}

带格式的: 字体: (中文) 黑体, 小四

带格式的: 标题 1

带格式的: 字体: 倾斜

带格式的: 下标

417 and σ was non-linear, mainly due to the variation of PNSD patterns (e.g., Andreae, 2009; Shinozuka
 418 et al., 2015). As discussed in section 3.3.1, SAE can be used to reflect the PNSD pattern. The clear
 419 vertical variation of SAE (Fig. 6a) suggests a complex and variable relationship between N_{CCN} at
 420 0.7% ~~SS~~-SS and σ at 450 nm at different altitudes. Shinozuka et al. (2015) identified N_{CCN} at 0.4+
 421 0.1% SS with $10^{0.3\alpha} \sigma_{ext}^{0.75}$ where σ_{ext} is the 500 nm extinction coefficient by dried particles and α is
 422 the extinction Angstrom exponent. Here, According to our measurements, the a modified
 423 parameterization provided by Shinozuka et al. (2015) is used in this study;

$$N_{CCN}=10^{\beta} \cdot \sigma^{\gamma} \quad (4)(3)$$

424 where σ is the aerosol scattering coefficient at 450 nm, and β and γ are two fitting parameters.
 425 Shinozuka et al. (2015) suggested that β and γ were correlated to SAE, but the degree of correlation
 426 differed in different regions. In this study, N_{CCN} at 0.7% ~~SS~~-SS and SAE data points are paired to
 427 derive β and γ . N_{CCN} at other ~~SS~~-SS levels are too little to do this work because of the loop
 428 measurement of different ~~SS~~-SS levels in the second column of CCNc-200.

429 Figure 7-S6 shows the relationships between SAE and β and SAE and γ in two air masses. β is
 430 negatively correlated with SAE, while γ is positively correlated with SAE. The correlation
 431 coefficients (R^2)s are lower (smaller coefficients of determination, R^2) in northwest~~erly~~ air masses
 432 than in southeast~~erly~~ air masses, likely due to more complex aerosol sources in northwest~~erly~~ air
 433 masses. Empirical estimates of N_{CCN} at 0.7% ~~SS~~-SS from aerosol optical properties are determined
 434 as follows:

$$\text{Northwest~~erly~~ air mass: } N_{CCN}=10^{-0.22 \cdot \text{SAE}+2.39} \cdot \sigma^{0.30 \cdot \text{SAE}+0.29} \quad (5)(4)$$

$$\text{Southeast~~erly~~ air mass: } N_{CCN}=10^{-0.07 \cdot \text{SAE}+2.29} \cdot \sigma^{0.14 \cdot \text{SAE}+0.28} \quad (6)(5)$$

435

- 带格式的: 字体: Times New Roman, 非倾斜
- 带格式的: 字体: Times New Roman, 非倾斜
- 带格式的: 字体: Times New Roman
- 带格式的: 字体: Times New Roman
- 带格式的: 字体: Times New Roman, 非倾斜
- 带格式的: 字体: Times New Roman, 非倾斜
- 带格式的: 字体: Times New Roman
- 带格式的: 字体: Times New Roman
- 带格式的: 字体颜色: 文字 1
- 带格式的: 字体: (中文) + 中文正文 (等线), 10 磅, 字体颜色: 自动设置

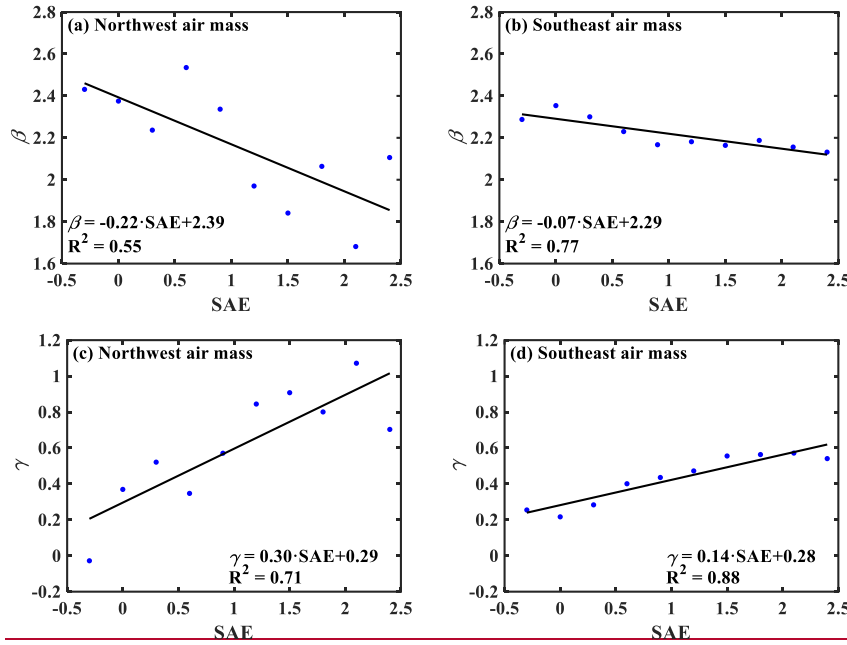


Figure 7. The two fitting parameters β and γ as a function of the aerosol scattering Ångström exponent (SAE) in northwest air masses (a and c) and southeast air masses (b and d). The dots are mean values averaged in 0.3-wide SAE bins. The black lines are best-fit lines from linear regression. Linear relations and coefficients of determination are given in each panel.

Figure 8-7 shows the comparisons of measured N_{CCN} at 0.7% $ss-SS$ and estimated N_{CCN} at 0.7% $ss-SS$ using Eqs. (4) and (5) for different vertical spiral flights in northwesterly and southwesterly air masses. For both air masses, most points approach the 1:1 line, indicating reasonable estimates using Eq. (4) and (5) to parameterize N_{CCN} . For northwesterly air masses (Fig. 8a7a), N_{CCN} estimates are better under high concentration conditions than under low concentration conditions. However, for southeasterly air masses (Fig. 7b), N_{CCN} estimates are better under low concentration conditions than under high concentration conditions. This is likely related to various aerosol sources at different altitudes. As previously discussed, most low N_{CCN} values are observed in the upper atmosphere above the TIL, while high N_{CCN} values are observed below the TIL. In northwesterly air masses, aerosol sources in the upper atmosphere are diverse, including the upward and long-distance transport of aerosols. This is why N_{CCN} estimates worsen under low N_{CCN} conditions. In southeasterly air masses, a single but thick TIL makes most aerosols accumulate in the lower

带格式的: 缩进: 首行缩进: 0 厘米

atmosphere, where local emissions and the impact of marine aerosols exacerbate N_{CCN} estimates. These results highlight the important impact of aerosol sources on the empirical estimate of N_{CCN} from aerosol optical properties.

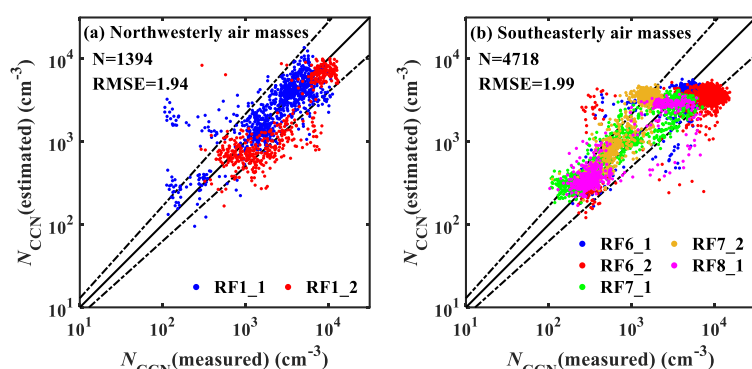


Figure 87. Comparisons between measured N_{CCN} at 0.7% $\omega\omega$ and estimated N_{CCN} at 0.7% $\omega\omega$ using Eqs. (4) and (5) for different vertical spiral flights in (a) northwesterly and (b) southeasterly air masses. The black solid lines are 1:1 line and the dash lines indicate the boundaries representing $\pm 10\%$ deviations of $N_{CCN}(\text{estimated})$ from $N_{CCN}(\text{measured})$ in the log-log plot. The 10% deviation means that the deviation of individual data points is typically within a factor of 1.26 of the best estimates. The point number (N) and root mean square error (RMSE) in each panel are given.

4. Conclusions

A comprehensive airborne campaign was conducted over the North China Plain (NCP) under the aegis of a project called Air chemistry Research In Asia (ARIAs). Seventy-two-hour air mass back trajectories show that the region of study during this campaign was mainly influenced by air masses from the arid/semi-arid regions to the northwest or air masses from the southeast associated with from and heavily populated and industrialized coastal or marine areas is mainly influenced by northwest and southeast air masses, originating from arid/semi-arid regions and coastal or marine areas, respectively. In this study, the profiles of cloud condensation nuclei number concentration (N_{CCN}) and their estimates from aerosol optical properties are analyzed.

It is We found that N_{CCN} profiles at the water vapor supersaturation ($\omega\omega$) of 0.7% are impacted largely by the temperature structure in the atmosphere. In general, the presence of a temperature

带格式的: 缩进: 首行缩进: 1.5 字符

带格式的: 字体: 五号, 非倾斜

带格式的: 字体: 五号

带格式的: 字体: 倾斜

带格式的: 字体: (中文) NimbusRomNo9L-Regu, 非突出显示

带格式的: 非突出显示

带格式的: 字体: (中文) NimbusRomNo9L-Regu, 非突出显示

带格式的: 非突出显示

inversion layer (TIL) suppresses the upward transport of aerosols from near the surface, which is affected by the number and thickness of TILs. In addition, air mass sources have a significant impact on N_{CCN} profile characteristics. Under the influence of northwesterly air masses, N_{CCN} in the free troposphere are easily impacted by the long-distance transport of aerosols. However, under the influence of southeasterly air masses, atmospheric thermal structures for all N_{CCN} profiles are similar, with one TIL present in all cases. The patterns of N_{CCN} profiles are also similar, showing much lower N_{CCN} above the TIL than near the surface. In addition to the impact of anthropogenic emissions, the transport of marine aerosols is another reason for the high N_{CCN} near the surface when a southeasterly air mass is present. Moreover, comparisons of N_{CCN} profiles during the same flights suggests that the terrain blocking effect of the Taihang Mountains on aerosols accumulates aerosols, resulting in high N_{CCN} near the mountains.

The Twomey's relation ($N_{CCN} = C \cdot (\sigma_{SS})^k$, where C and k are two fitting coefficients) is used to analyze CCN spectra and aerosol activation ability in this study. In general, there is a clear change in CCN spectra with altitude. The aerosol activation ability in southeasterly air masses is stronger than in northwesterly air masses, mainly due to the different chemical composition associated with diverse air masses. In addition, the aerosol activation ability is stronger in the free atmosphere than near the surface. The hindering effect of a TIL on the upward transport of aerosols promotes aerosol aging processes, enhancing the aerosol activation ability near the TIL. The vertical distribution of aerosol scattering Ångström exponent (SAE) indicates that aerosols near the surface are easily influenced by primary emissions, consisting of more fine particles. The combined effect of aerosol upward and long-distance transport increases SAE and make it vary more in the free troposphere than near the surface.

The comparison of N_{CCN} at 0.7% σ_{SS} and aerosol scattering coefficient (σ) at 450 nm suggests that the vertical variation of σ is synchronous with that of N_{CCN} . The equation, $N_{CCN} = 10^{\beta} \cdot \sigma^{\gamma}$ (β and γ are two fitting parameters), is used to parameterize N_{CCN} , with the parameters β and γ being linearly correlated with the SAE. Empirical estimates of N_{CCN} at 0.7% σ_{SS} from aerosol optical properties are thus retrieved ($N_{CCN} = 10^{-0.22 \cdot SAE + 2.39} \cdot \sigma^{0.30 \cdot SAE + 0.29}$ for northwesterly air masses, and $N_{CCN} = 10^{-0.07 \cdot SAE + 2.29} \cdot \sigma^{0.14 \cdot SAE + 0.28}$ for southeasterly air masses). The closure between the estimated and measured N_{CCN} at 0.7% σ_{SS} is acceptable although different performances are seen under low and high concentration conditions for the two air masses. Results suggest the important impact of

aerosol sources on the empirical estimate of N_{CCN} from aerosol optical properties.

N_{CCN} profiles in the NCP are impacted by multiple factors, including temperature structure, air mass sources, anthropogenic emissions, and terrain distribution. These factors make estimating N_{CCN} from aerosol optical properties more difficult. In the future, more aircraft measurement data will be needed to establish a more reasonable parameterization scheme for N_{CCN} at different ss . This study may also be useful for studying aerosol activation ability in other regions of the world.

Acknowledgements. This work was funded by the National Natural Science Foundation of China (NSFC) research projects (grant nos. 42005067, ~~and~~ 42030606, ~~and~~ 92044303), the National Science Foundation of the United States (grant no. 1558259). We also thank all participants in the campaign for their tireless work and cooperation, especially the ~~work help of from~~ the Hebei Weather Modification Office.

Data availability. Measurement data from the field campaign used in this study are available from the corresponding author upon request (yuyingwang@nuist.edu.cn).

Author contributions. ZL and YW determined the main goal of this study. RZ and YW conceived the study and prepared this paper. ZL, RD, HS, and YC led the airborne campaign, ZW, XR, HH, and FW conducted this airborne campaign. HS, YC, and ZW provided the CCN data. YG, XC, and JX processed the measurement data. All co-authors participated in science discussions and suggested analyses.

Competing interests. The authors declare that they have no conflict of interest.

5. References

- Anderson, T. L. and Ogren, J. A.: Determining aerosol radiative properties using the TSI 3563 integrating nephelometer, *Aerosol Science and Technology*, 29, 57-69, <https://doi.org/10.1080/02786829808965551>, 1998.
- Andreae, M. O.: Correlation between cloud condensation nuclei concentration and aerosol optical thickness in remote and polluted regions, *Atmospheric Chemistry and Physics*, 9, 543-556, <https://doi.org/10.5194/acp-9-543-2009>, 2009.

- Andreae, M. O. and Rosenfeld, D.: Aerosol–cloud–precipitation interactions. Part 1. The nature and sources of cloud-active aerosols, *Earth-Science Reviews*, 89, 13-41, <https://doi.org/10.1016/j.earscirev.2008.03.001>, 2008.
- [Benish, S. E., He, H., Ren, X., Roberts, S. J., Salawitch, R. J., Li, Z., Wang, F., Wang, Y., Zhang, F., Shao, M., Lu, S., and Dickerson, R. R.: Measurement report: Aircraft observations of ozone, nitrogen oxides, and volatile organic compounds over Hebei Province, China, *Atmospheric Chemistry and Physics Atmos. Chem. Phys.*, 20, 14523-14545, <https://doi.org/10.5194/acp-20-14523-2020>, 2020.](#)
- [Benish, S. E., Salawitch, R. J., Ren, X., He, H., and Dickerson, R. R.: Airborne Observations of CFCs Over Hebei Province, China in Spring 2016, *Journal of Geophysical Research: Atmospheres*, 126, e2021J-c35152J, <https://doi.org/10.1029/2021JD035152>, 2021.](#)
- Bond, T. C., Doherty, S. J., Fahey, D. W., Forster, P. M., Bernsten, T., DeAngelo, B. J., Flanner, M. G., Ghan, S., Kärcher, B., Koch, D., Kinne, S., Kondo, Y., Quinn, P. K., Sarofim, M. C., Schultz, M. G., Schulz, M., Venkataraman, C., Zhang, H., Zhang, S., Bellouin, N., Guttikunda, S. K., Hopke, P. K., Jacobson, M. Z., Kaiser, J. W., Klimont, Z., Lohmann, U., Schwarz, J. P., Shindell, D., Storelvmo, T., Warren, S. G., and Zender, C. S.: Bounding the role of black carbon in the climate system: A scientific assessment, *Journal of Geophysical Research: Atmospheres*, 118, 5380-5552, <https://doi.org/10.1002/jgrd.50171>, 2013.
- Cai, M., Tan, H., Chan, C. K., Qin, Y., Xu, H., Li, F., Schurman, M. I., Liu, L., and Zhao, J.: The size-resolved cloud condensation nuclei (CCN) activity and its prediction based on aerosol hygroscopicity and composition in the Pearl Delta River (PRD) region during wintertime 2014, *Atmospheric Chemistry and Physics*, 18, 16,419-16,437, <https://doi.org/10.5194/acp-18-16419-2018>, 2018.
- Cai, Z., Li, Z., Li, P., Li, J., Sun, H., Yang, Y., Gao, X., Ren, G., Ren, R., and Wei, J.: Vertical distributions of aerosol microphysical and optical properties based on aircraft measurements made over the Loess Plateau in China, *Atmospheric Environment*, 270, 118888, <https://doi.org/10.1016/j.atmosenv.2021.118888>, 2022.
- Chen, C., Qiu, Y., Xu, W., He, Y., Li, Z., Sun, J., Ma, N., Xu, W., Pan, X., Fu, P., Wang, Z., and Sun, Y.: Primary emissions and secondary aerosol processing during wintertime in rural area of North China Plain, *Journal of Geophysical Research: Atmospheres*, 127, e2021JD035430, <https://doi.org/10.1029/2021JD035430>, 2022.
- [Choudhury, G., and Tesche, M.: Estimating cloud condensation nuclei concentrations from CALIPSO lidar measurements, *Atmospheric Measurement Techniques Atmos. Meas. Tech.*, 15, 639-654, <https://doi.org/10.5194/amt-15-639-2022>, 2022.](#)
- Cohard, J.-M., Pinty, J.-P., and Bedos, C.: Extending Twomey's analytical estimate of nucleated cloud droplet concentrations from CCN spectra, *Journal of the Atmospheric Sciences*, 55, 3348-3357, [https://doi.org/10.1175/1520-0469\(1998\)055<3348:Etsao>2.0.Co;2](https://doi.org/10.1175/1520-0469(1998)055<3348:Etsao>2.0.Co;2), 1998.
- ~~Draxier, R. R. and Hess, G. D.: An overview of the HYSPLIT_4 modeling system of trajectories, dispersion, and deposition, *Australian Meteorological Magazine*, 47, 295-308, 1998.~~
- Fan, J., Wang, Y., Rosenfeld, D., and Liu, X.: Review of aerosol–cloud interactions: mechanisms, significance, and challenges, *Journal of the Atmospheric Sciences*, 73, 4221-4252, <https://doi.org/10.1175/jas-d-16-0037.1>, 2016.
- Farmer, D. K., Cappa, C. D., and Kreidenweis, S. M.: Atmospheric processes and their controlling influence on cloud condensation nuclei activity, *Chemical Reviews*, 115, 4199-4217, <https://doi.org/10.1021/cr5006292>, 2015.

带格式的: 字体: (默认) Times New Roman, (中文) 等线, 10磅, 字体颜色: 文字 1, 英语(美国)

带格式的: EndNote Bibliography, 缩进: 左侧: 0 厘米, 悬挂缩进: 2 字符, 右侧: 0 厘米, 首行缩进: -2 字符, 定义网格后自动调整右缩进, 调整中文与西文文字的间距, 调整中文与数字的间距

带格式的: 字体: (默认) Times New Roman, (中文) 等线, 10磅, 字体颜色: 文字 1, 英语(美国)

带格式的: 字体: (默认) Times New Roman, (中文) 等线, 10磅, 字体颜色: 文字 1, 英语(美国)

带格式的: 缩进: 左侧: 0 厘米, 悬挂缩进: 2 字符

带格式的: 字体: (默认) Times New Roman, (中文) 等线, 10磅, 字体颜色: 文字 1, 英语(美国)

带格式的: 缩进: 左侧: 0 厘米, 悬挂缩进: 2 字符

带格式的: 字体: (默认) Times New Roman, (中文) 等线, 10磅, 字体颜色: 文字 1, 英语(美国)

带格式的: 字体: (默认) Times New Roman, (中文) 等线, 10磅, 字体颜色: 文字 1, 英语(美国)

- Gunthe, S. S., Rose, D., Su, H., Garland, R. M., Achtert, P., Nowak, A., Wiedensohler, A., Kuwata, M., Takegawa, N., Kondo, Y., Hu, M., Shao, M., Zhu, T., Andreae, M. O., and Pöschl, U.: Cloud condensation nuclei (CCN) from fresh and aged air pollution in the megacity region of Beijing, *Atmospheric Chemistry and Physics*, 11, 11,023-11,039, <https://doi.org/10.5194/acp-11-11023-2011>, 2011.
- Guo, L. J., Guo, X. L., Fang, C. G., and Zhu, S. C.: Observation analysis on characteristics of formation, evolution and transition of a long-lasting severe fog and haze episode in North China, *Science China-Earth Sciences*, 58, 329-344, <https://doi.org/10.1007/s11430-014-4924-2>, 2015.
- Hamonou, E., Chazette, P., Balis, D., Dulac, F., Schneider, X., Galani, E., Ancellet, G., and Papayannis, A.: Characterization of the vertical structure of Saharan dust export to the Mediterranean basin, *Journal of Geophysical Research: Atmospheres*, 104, 22,257-22,270, <https://doi.org/10.1029/1999jd900257>, 1999.
- Hegg, D. A., Radke, L. F., and Hobbs, P. V.: Measurements of Aitken nuclei and cloud condensation nuclei in the marine atmosphere and their relation to the DMS-Cloud-climate hypothesis, *Journal of Geophysical Research: Atmospheres*, 96, 18,727-18,733, <https://doi.org/10.1029/91JD01870>, 1991.
- IPCC. Climate Change 2021: The physical basis, sixth assessment of the Inter-governmental Panel on Climate Change[M]. Cambridge University Press, 2021.
- Janhäll, S., Olofson, K. F. G., Andersson, P. U., Pettersson, J. B. C., and Hallquist, M.: Evolution of the urban aerosol during winter temperature inversion episodes, *Atmospheric Environment*, 40, 5355-5366, <https://doi.org/10.1016/j.atmosenv.2006.04.051>, 2006.
- Jayachandran, V. N., Suresh Babu, S. N., Vaishya, A., Gogoi, M. M., Nair, V. S., Satheesh, S. K., and Krishna Moorthy, K.: Altitude profiles of cloud condensation nuclei characteristics across the Indo-Gangetic Plain prior to the onset of the Indian summer monsoon, *Atmospheric Chemistry and Physics*, 20, 561-576, <https://doi.org/10.5194/acp-20-561-2020>, 2020a.
- Jayachandran, V. N., Varghese, M., Murugavel, P., Todekar, K. S., Bankar, S. P., Malap, N., Dinesh, G., Safai, P. D., Rao, J., Konwar, M., Dixit, S., and Prabha, T. V.: Cloud condensation nuclei characteristics during the Indian summer monsoon over a rain-shadow region, *Atmospheric Chemistry and Physics*, 20, 7307-7334, <https://doi.org/10.5194/acp-20-7307-2020>, 2020b.
- Jefferson, A.: Empirical estimates of CCN from aerosol optical properties at four remote sites, *Atmospheric Chemistry and Physics*, 10, 6855-6861, <https://doi.org/10.5194/acp-10-6855-2010>, 2010.
- Ji, Q. and Shaw, G. E.: On supersaturation spectrum and size distributions of cloud condensation nuclei, *Geophysical Research Letters*, 25, 1903-1906, <https://doi.org/10.1029/98GL01404>, 1998.
- Juranyi, Z., Gysel, M., Weingartner, E., Bukowiecki, N., Kammermann, L., and Baltensperger, U.: A 17 month climatology of the cloud condensation nuclei number concentration at the high alpine site Jungfraujoch, *Journal of Geophysical Research: Atmospheres*, 116, <https://doi.org/10.1029/2010JD015199>, 2011.
- Leng, C. P., Cheng, T. T., Chen, J. M., Zhang, R. J., Tao, J., Huang, G. H., Zha, S. P., Zhang, M. G., Fang, W., Li, X., and Li, L.: Measurements of surface cloud condensation nuclei and aerosol activity in downtown Shanghai, *Atmospheric Environment*, 69, 354-361, <https://doi.org/10.1016/j.atmosenv.2012.12.021>, 2013.
- Li, J., Chen, H., Li, Z., Wang, P., Cribb, M., and Fan, X.: Low-level temperature inversions and their effect on aerosol condensation nuclei concentrations under different large-scale synoptic

627 circulations, *Advances in Atmospheric Sciences*, 32, 898-908, [https://doi.org/10.1007/s00376-014-](https://doi.org/10.1007/s00376-014-4150-z)
628 4150-z, 2015a.

629 Li, J., Yin, Y., Li, P., Li, Z., Li, R., Cribb, M., Dong, Z., Zhang, F., Li, J., Ren, G., Jin, L., and Li, Y.:
630 Aircraft measurements of the vertical distribution and activation property of aerosol particles over
631 the Loess Plateau in China, *Atmospheric Research*, 155, 73-86,
632 <https://doi.org/10.1016/j.atmosres.2014.12.004>, 2015b.

633 Li, Z., Lau, W. K.-M., Ramanathan, V., Wu, G., Ding, Y., Manoj, M. G., Liu, J., Qian, Y., Li, J., Zhou, T.,
634 Fan, J., Rosenfeld, D., Ming, Y., Wang, Y., Huang, J., Wang, B., Xu, X., Lee, S.-S., Cribb, M., Zhang,
635 F., Yang, X., Zhao, C., Takemura, T., Wang, K., Xia, X., Yin, Y., Zhang, H., Guo, J., Zhai, P. M.,
636 Sugimoto, N., Babu, S. S., and Brasseur, G. P.: Aerosol and monsoon climate interactions over Asia,
637 *Reviews of Geophysics*, 54, 866-929, <https://doi.org/10.1002/2015RG000500>, 2016.

638 Li, Z., Wang, Y., Guo, J., Zhao, C., Cribb, M. C., Dong, X., Fan, J., Gong, D., Huang, J., Jiang, M., Jiang,
639 Y., Lee, S. S., Li, H., Li, J., Liu, J., Qian, Y., Rosenfeld, D., Shan, S., Sun, Y., Wang, H., Xin, J., Yan,
640 X., Yang, X., Yang, X.-Q., Zhang, F., and Zheng, Y.: East Asian Study of Tropospheric Aerosols and
641 their Impact on Regional Clouds, Precipitation, and Climate (EAST-AIRCPC), *Journal of*
642 *Geophysical Research: Atmospheres*, 124, 13,026-13,054, <https://doi.org/10.1029/2019JD030758>,
643 2019.

644 Liu, J. and Li, Z.: Estimation of cloud condensation nuclei concentration from aerosol optical quantities:
645 influential factors and uncertainties, *Atmospheric Chemistry and Physics*, 14, 471-483,
646 <https://doi.org/10.5194/acp-14-471-2014>, 2014.

647 Liu, L., Cheng, Y., Wang, S., Wei, C., Pöhlker, M. L., Pöhlker, C., Artaxo, P., Shrivastava, M., Andreae,
648 M. O., Pöschl, U., and Su, H.: Impact of biomass burning aerosols on radiation, clouds, and
649 precipitation over the Amazon: relative importance of aerosol-cloud and aerosol-radiation
650 interactions, *Atmospheric Chemistry and Physics*, 20, 13283-13301, [https://doi.org/10.5194/acp-](https://doi.org/10.5194/acp-20-13283-2020)
651 20-13283-2020, 2020.

652 Lohmann, U. and Feichter, J.: Global indirect aerosol effects: a review, *Atmospheric Chemistry and*
653 *Physics*, 5, 715-737, <https://doi.org/10.5194/acp-5-715-2005>, 2005.

654 Lv, M., Wang, Z., Li, Z., Luo, T., Ferrare, R., Liu, D., Wu, D., Mao, J., Wan, B., Zhang, F., and Wang, Y.:
655 Retrieval of Cloud Condensation Nuclei Number Concentration Profiles From Lidar Extinction and
656 Backscatter Data, *Journal of Geophysical Research: Atmospheres*, 123, 6082-6098,
657 <https://doi.org/10.1029/2017JD028102>, 2018.

658 Mamouri, R. E., and Ansmann, A.: Potential of polarization lidar to provide profiles of CCN- and INP-
659 relevant aerosol parameters, *Atmospheric Chemistry and Physics*, 16, 5905-
660 5931, <https://doi.org/10.5194/acp-16-5905-2016>, 2016.

661 Manoj, M. R., Satheesh, S. K., Moorthy, K. K., Trembath, J., and Coe, H.: Measurement report:
662 Altitudinal variation of cloud condensation nuclei activation across the Indo-Gangetic Plain prior to
663 monsoon onset and during peak monsoon periods: results from the SWAAMI field campaign,
664 *Atmospheric Chemistry and Physics*, 21, 8979-8997, <https://doi.org/10.5194/acp-21-8979-2021>,
665 2021.

666 Paramonov, M., Kerminen, V. M., Gysel, M., Aalto, P. P., Andreae, M. O., Asmi, E., Baltensperger, U.,
667 Bougiatioti, A., Brus, D., Frank, G. P., Good, N., Gunthe, S. S., Hao, L., Irwin, M., Jaatinen, A.,
668 Juranyi, Z., King, S. M., Kortelainen, A., Kristensson, A., Lihavainen, H., Kulmala, M., Lohmann,
669 U., Martin, S. T., McFiggans, G., Mihalopoulos, N., Nenes, A., O'Dowd, C. D., Ovadnevaite, J.,
670 Petaja, T., Poschl, U., Roberts, G. C., Rose, D., Svenningsson, B., Swietlicki, E., Weingartner, E.,

带格式的: 字体: (默认) Times New Roman, (中文) 等线, 10磅, 字体颜色: 文字 1, 英语(美国)

带格式的: 缩进: 左侧: 0 厘米, 悬挂缩进: 2 字符

带格式的: 字体: (默认) Times New Roman, (中文) 等线, 10磅, 字体颜色: 文字 1, 英语(美国)

带格式的: 字体: (默认) Times New Roman, (中文) 等线, 10磅, 字体颜色: 文字 1, 英语(美国)

带格式的: 字体: (默认) Times New Roman, (中文) 等线, 10磅, 字体颜色: 文字 1, 英语(美国)

带格式的: 字体: (默认) Times New Roman, (中文) 等线, 10磅, 字体颜色: 文字 1, 英语(美国)

- Whitehead, J., Wiedensohler, A., Wittbom, C., and Sierau, B.: A synthesis of cloud condensation nuclei counter (CCNC) measurements within the EUCAARI network, *Atmospheric Chemistry and Physics*, 15, 12,211-12,229, <https://doi.org/10.5194/acp-15-12211-2015>, 2015.
- Ren, J., Zhang, F., Wang, Y., Collins, D., Fan, X., Jin, X., Xu, W., Sun, Y., Cribb, M., and Li, Z.: Using different assumptions of aerosol mixing state and chemical composition to predict CCN concentrations based on field measurements in urban Beijing, *Atmospheric Chemistry and Physics*, 18, 6907-6921, <https://doi.org/10.5194/acp-18-6907-2018>, 2018.
- Ren, R., Li, Z., Yan, P., Wang, Y., Wu, H., Cribb, M., Wang, W., Jin, X., Li, Y., and Zhang, D.: Measurement report: The effect of aerosol chemical composition on light scattering due to the hygroscopic swelling effect, *Atmospheric Chemistry and Physics*, 21, 9977-9994, <https://doi.org/10.5194/acp-21-9977-2021>, 2021.
- Rose, D., Gunthe, S. S., Mikhailov, E., Frank, G. P., Dusek, U., Andreae, M. O., and Pöschl, U.: Calibration and measurement uncertainties of a continuous-flow cloud condensation nuclei counter (DMT-CCNC): CCN activation of ammonium sulfate and sodium chloride aerosol particles in theory and experiment, *Atmospheric Chemistry and Physics*, 8, 1153-1179, <https://doi.org/10.5194/acp-8-1153-2008>, 2008.
- Rose, D., Nowak, A., Achtert, P., Wiedensohler, A., Hu, M., Shao, M., Zhang, Y., Andreae, M. O., and Pöschl, U.: Cloud condensation nuclei in polluted air and biomass burning smoke near the megacity Guangzhou, China – Part 1: Size-resolved measurements and implications for the modeling of aerosol particle hygroscopicity and CCN activity, *Atmospheric Chemistry and Physics*, 10, 3365-3383, <https://doi.org/10.5194/acp-10-3365-2010>, 2010.
- Rosenfeld, D., Lohmann, U., Raga, G. B., O'Dowd, C. D., Kulmala, M., Fuzzi, S., Reissell, A., and Andreae, M. O.: Flood or drought: How do aerosols affect precipitation?, *Science*, 321, 1309-1313, <https://doi.org/10.1126/science.1160606>, 2008.
- Rosenfeld, D., Sherwood, S., Wood, R., and Donner, L.: Climate effects of aerosol-cloud interactions, *Science*, 343, 379-380, <https://doi.org/10.1126/science.1247490>, 2014.
- Rosenfeld, D., Zheng, Y., Hashimshoni, E., Pöhlker, M. L., Jefferson, A., Pöhlker, C., Yu, X., Zhu, Y., Liu, G., Yue, Z., Fischman, B., Li, Z., Giguzin, D., Goren, T., Artaxo, P., Barbosa, H. M. J., Pöschl, U., and Andreae, M. O.: Satellite retrieval of cloud condensation nuclei concentrations by using clouds as CCN chambers, *Proceedings of the National Academy of Sciences USA*, 113, 5828-5834, <https://doi.org/10.1073/pnas.1514044113>, 2016.
- Schmale, J., Henning, S., Decesari, S., Henzing, B., Keskinen, H., Sellegri, K., Ovadnevaite, J., Pöhlker, M. L., Brito, J., Bougiatioti, A., Kristensson, A., Kalivitis, N., Stavroulas, I., Carbone, S., Jefferson, A., Park, M., Schlag, P., Iwamoto, Y., Aalto, P., Aijala, M., Bukowiecki, N., Ehn, M., Frank, G., Frohlich, R., Frumau, A., Herrmann, E., Herrmann, H., Holzinger, R., Kos, G., Kulmala, M., Mihalopoulos, N., Nenes, A., O'Dowd, C., Petaja, T., Picard, D., Pöhlker, C., Pöschl, U., Poulain, L., Prevot, A. S. H., Swietlicki, E., Andreae, M. O., Artaxo, P., Wiedensohler, A., Ogren, J., Matsuki, A., Yum, S. S., Stratmann, F., Baltensperger, U., and Gysel, M.: Long-term cloud condensation nuclei number concentration, particle number size distribution and chemical composition measurements at regionally representative observatories, *Atmospheric Chemistry and Physics*, 18, 2853-2881, <https://doi.org/10.5194/acp-18-2853-2018>, 2018.
- Shinozuka, Y., Clarke, A. D., Nenes, A., Jefferson, A., Wood, R., McNaughton, C. S., Ström, J., Tunved, P., Redemann, J., Thornhill, K. L., Moore, R. H., Latham, T. L., Lin, J. J., and Yoon, Y. J.: The relationship between cloud condensation nuclei (CCN) concentration and light extinction of dried

- particles: indications of underlying aerosol processes and implications for satellite-based CCN estimates, *Atmospheric Chemistry and Physics*, 15, 7585-7604, <https://doi.org/10.5194/acp-15-7585-2015>, 2015.
- Stein, A. F., Draxler, R. R., Rolph, G. D., Stunder, B. J. B., Cohen, M. D., and Ngan, F.: NOAA's HYSPLIT Atmospheric Transport and Dispersion Modeling System, *Bulletin of the American Meteorological Society*, 96, 2059-2077, <https://doi.org/10.1175/BAMS-D-14-00110.1>, 2015.
- Tao, J., Zhao, C., Kuang, Y., Zhao, G., Shen, C., Yu, Y., Bian, Y., and Xu, W.: A new method for calculating number concentrations of cloud condensation nuclei based on measurements of a three-wavelength humidified nephelometer system, *Atmospheric Measurement Techniques*, 11, 895-906, <https://doi.org/10.5194/amt-11-895-2018>, 2018.
- Twomey, S.: The nuclei of natural cloud formation. Part II: The supersaturation in natural clouds and the variation of cloud droplet concentration, *Geofisica pura e applicata*, 43, 243-249, <https://doi.org/10.1007/BF01993560>, 1959.
- Wang, F., Li, Z., Ren, X., Jiang, Q., He, H., Dickerson, R. R., Dong, X., and Lv, F.: Vertical distributions of aerosol optical properties during the spring 2016 ARIAs airborne campaign in the North China Plain, *Atmospheric Chemistry and Physics*, 18, 8995-9010, <https://doi.org/10.5194/acp-18-8995-2018>, 2018.
- Wang, Q., Du, W., Sun, Y., Wang, Z., Tang, G., and Zhu, J.: Submicron-scale aerosol above the city canopy in Beijing in spring based on in-situ meteorological tower measurements, *Atmospheric Research*, 271, 106128, <https://doi.org/10.1016/j.atmosres.2022.106128>, 2022.
- Wang, Y., Li, Z., Zhang, Y., Du, W., Zhang, F., Tan, H., Xu, H., Fan, T., Jin, X., Fan, X., Dong, Z., Wang, Q., and Sun, Y.: Characterization of aerosol hygroscopicity, mixing state, and CCN activity at a suburban site in the central North China Plain, *Atmospheric Chemistry and Physics*, 18, 11739-11752, <https://doi.org/10.5194/acp-18-11739-2018>, 2018.
- Wang, Y., Dörner, S., Donner, S., Böhne, S., De Smedt, I., Dickerson, R. R., Dong, Z., He, H., Li, Z., Li, Z., Li, D., Liu, D., Ren, X., Theys, N., Wang, Y., Wang, Y., Wang, Z., Xu, H., Xu, J., and Wagner, T.: Vertical profiles of NO₂, SO₂, HONO, HCHO, CHOCHO and aerosols derived from MAX-DOAS measurements at a rural site in the central western North China Plain and their relation to emission sources and effects of regional transport, *Atmospheric Chemistry and Physics*, 19, 5417-5449, <https://doi.org/10.5194/acp-19-5417-2019>, 2019.
- Xia, C., Sun, J., Qi, X., Shen, X., Zhong, J., Zhang, X., Wang, Y., Zhang, Y., and Hu, X.: Observational study of aerosol hygroscopic growth on scattering coefficient in Beijing: A case study in March of 2018, *Science of The Total Environment*, 685, 239-247, <https://doi.org/10.1016/j.scitotenv.2019.05.283>, 2019.
- Xu, W., Ovadnevaite, J., Fossun, K. N., Lin, C. S., Huang, R. J., O'Dowd, C., and Ceburnis, D.: Aerosol hygroscopicity and its link to chemical composition in the coastal atmosphere of Mace Head: marine and continental air masses, *Atmospheric Chemistry and Physics*, 20, 3777-3791, <https://doi.org/10.5194/acp-20-3777-2020>, 2020.
- Yau, M. K., and Rogers, R. R.: A short course in cloud physics, edited, Elsevier, 1996.
- Zhang, F., Li, Z. Q., Li, Y. A., Sun, Y. L., Wang, Z. Z., Li, P., Sun, L., Wang, P. C., Cribb, M., Zhao, C. F., Fan, T. Y., Yang, X., and Wang, Q. Q.: Impacts of organic aerosols and its oxidation level on CCN activity from measurement at a suburban site in China, *Atmospheric Chemistry and Physics*, 16, 5413-5425, <https://doi.org/10.5194/acp-16-5413-2016>, 2016.

带格式的: 字体: (默认) Times New Roman, (中文) 等线, 10磅, 字体颜色: 文字 1, 英语(美国)

带格式的: 缩进: 左侧: 0 厘米, 悬挂缩进: 2 字符

带格式的: 字体: (默认) Times New Roman, (中文) 等线, 10磅, 字体颜色: 文字 1, 英语(美国)

带格式的: 字体: (默认) Times New Roman, (中文) 等线, 10磅, 字体颜色: 文字 1, 英语(美国)

带格式的: 字体: (默认) Times New Roman, (中文) 等线, 10磅, 字体颜色: 文字 1, 英语(美国)

带格式的: 缩进: 左侧: 0 厘米, 悬挂缩进: 2 字符

带格式的: 字体: (默认) Times New Roman, (中文) 等线, 10磅, 字体颜色: 文字 1, 英语(美国)

带格式的: 字体: (默认) Times New Roman, (中文) 等线, 10磅, 字体颜色: 文字 1, 英语(美国)

759 Zhang, F., Wang, Y. Y., Peng, J. F., Ren, J. Y., Collins, D., Zhang, R. Y., Sun, Y. L., Yang, X., and Li, Z.
760 Q.: Uncertainty in predicting CCN activity of aged and primary aerosols, *Journal of Geophysical*
761 *Research: Atmospheres*, 122, 11,723-11,736, <https://doi.org/10.1002/2017jd027058>, 2017.
762 Zhang, L., Sun, J. Y., Shen, X. J., Zhang, Y. M., Che, H., Ma, Q. L., Zhang, Y. W., Zhang, X. Y., and
763 Ogren, J. A.: Observations of relative humidity effects on aerosol light scattering in the Yangtze
764 River Delta of China, *Atmospheric Chemistry and Physics*, 15, 8439-8454,
765 <https://doi.org/10.5194/acp-15-8439-2015>, 2015.

带格式的: 缩进: 左侧: 0 厘米, 首行缩进: 0 字符